nature chemistry

ARTICLES

https://doi.org/10.1038/s41557-019-0406-7

Branched kissing loops for the construction of diverse RNA homooligomeric nanostructures

Di Liu[1], Cody W. Geary[2,3], Gang Chen[1,7], Yaming Shao[4], Mo Li[5], Chengde Mao[5], Ebbe S. Andersen[2], Joseph A. Piccirilli[1,4], Paul W. K. Rothemund[3*] and Yossi Weizmann[1,6*]

In biological systems, large and complex structures are often assembled from multiple simpler identical subunits. This strategy—homooligomerization—allows efficient genetic encoding of structures and avoids the need to control the stoichiometry of multiple distinct units. It also allows the minimal number of distinct subunits when designing artificial nucleic acid structures. Here, we present a robust self-assembly system in which homooligomerizable tiles are formed from intramolecularly folded RNA single strands. Tiles are linked through an artificially designed branched kissing-loop motif, involving Watson–Crick base pairing between the single-stranded regions of a bulged helix and a hairpin loop. By adjusting the tile geometry to gain control over the curvature, torsion and the number of helices, we have constructed 16 different linear and circular structures, including a finite-sized three-dimensional cage. We further demonstrate cotranscriptional self-assembly of tiles based on branched kissing loops, and show that tiles inserted into a transfer RNA scaffold can be overexpressed in bacterial cells.

Large and complex structures are often required to fulfil the sophisticated functions of biological systems. Although scale and complexity can be achieved through expressing a single long chain—most notably the protein titin[1], the largest isoform of which comprises a concatemer of 244 similar subunits with a total of 33,000 amino acids—a considerable fraction of large protein structures are instead constructed as oligomers from many identical subunits[2–4]. Proposed advantages[2] of such homooligomeric proteins include high genetic coding efficiency, reduced translation errors and intricate regulation of assembly (such as the dynamic instability and treadmilling of microtubules[5] and actin filaments[6]). Reasonably, there is a length scale above which nature ceases to create finite structures whose sizes are explicitly coded by gene length, and instead employs identical subunits to create structures whose sizes are implicitly encoded by the geometry of the subunit (for example, the size of an oligomeric ring is dictated by the geometry of its constituent monomers[2]) or are controlled by a system of complex regulation (for example, many different structures, of different sizes, can be made from the same subunit as required by particular cellular contexts—actin structures within the pseudopod of a moving macrophage are very different than those within the muscle sarcomere[7]).

Constructing artificial homooligomeric self-assembly systems with a structural diversity that rivals those found in nature remains an important challenge for both nanoscience and chemical biology. The extraordinary programmability of nucleic acid hybridization, as demonstrated by a wide variety of advanced artificial nanoarchitectures[8–11], makes nucleic acids attractive materials for building such systems. Moreover, natural homooligomeric systems based on nucleic acids play a number of important roles, such as forming the dimer linkage structure in retroviral genomic RNA[12] and creating a ring of prohead RNA (pRNA) in the packaging motor of Φ29-like bacteriophages[13]. A better understanding of these natural systems might be reached by constructing and analysing their artificial counterparts.

Identical subunits (known as 'tiles') for assembling large extended structures can be created from multiple strands of DNA[14,15] or RNA[16]. However, to prevent the formation of incomplete tiles, which might result in defects or chain termination, it is important to tightly control the stoichiometry of the different constituent strands. One way to evade this requirement is to construct each tile using a single strand. A number of systems have partly explored this approach with DNA[17–19] or RNA[20–22]. For DNA, two difficulties have prevented the widespread design of one-stranded homooligomeric assemblies. First, despite recent advances, the high-yield synthesis of sufficiently long single-stranded (ss) DNA remains relatively challenging and/or expensive, either by phosphoramidite-based chemical synthesis, phage-based biological production[23] or various enzymatic methods[24–27]. Second, DNA-based designs typically require multiple distinct strands to provide the free ss ends ('sticky ends') or patterns of blunt ends[28,29] necessary for cohesive interactions between subunits. Clever use of sequence symmetry can partly solve both difficulties, and tiles can be designed to be formed by two identical copies of a short strand containing palindromic segments[17–19]. However, the geometries that can be accessed by such sequence-symmetry tricks seem limited.

Compared with DNA, RNA has a greater capacity for functions and more facile in vitro and in vivo synthesis; such features make RNA nanotechnology an exciting emerging field[11,30]. Partly guided by concepts from DNA nanotechnology, a wide assortment of RNA constructs, including topological structures[31,32], polyhedra[33], tile-based assemblies[16] and origami-like structures[22,34,35], have been created. Further, natural RNAs have a cornucopia of structural primitives that can be mined to increase the structural diversity of artificial nanoarchitectures. In fact, the use of natural RNA folds (such as tRNA[36] and pRNA[37–39]) and motifs (such as bulges[40,41],

---

[1]Department of Chemistry, University of Chicago, Chicago, IL, USA. [2]Interdisciplinary Nanoscience Center and Department of Molecular Biology and Genetics, Aarhus University, Aarhus, Denmark. [3]Departments of Bioengineering, Computational and Mathematical Sciences, and Computation and Neural Systems, California Institute of Technology, Pasadena, CA, USA. [4]Department of Biochemistry and Molecular Biology, University of Chicago, Chicago, IL, USA. [5]Department of Chemistry, Purdue University, West Lafayette, IN, USA. [6]Department of Chemistry, Ben-Gurion University of the Negev, Beer-Sheva, Israel. [7]Present address: Department of Chemistry, University of Central Florida, Orlando, FL, USA. *e-mail: pwkr@dna.caltech.edu; yweizmann@bgu.ac.il

kink-turns[42], junctions[43] and kissing loops (KLs)[44]) have provided the basis for an important strain of RNA nanotechnology known as RNA tectonics or tectoRNA[45–47], which emphasizes the combination of the unique geometries of multiple natural folds/motifs to arrive at a desired shape. Practiced in its most complex form, RNA tectonics has enabled the cotranscriptional production of sophisticated shapes including a heart[47]. Meanwhile, RNA has been used to build a number of homooligomeric assembly systems by taking advantage of two facts: (1) long ssRNA can be easily obtained by in vitro transcription from readily accessible double-stranded DNA templates; and (2) naturally occurring paranemic motifs, such as the tetraloop/tetraloop-receptor[21] and KL[20,22,48,49] interactions, can provide the cohesion necessary for oligomerization without depending on free ends. Nevertheless, the small vocabulary of geometries available to natural motifs has limited the structural diversity of RNA homooligomeric systems.

In this work, we present a homooligomeric self-assembly system based on an artificially designed branched KL (bKL) motif. This bKL is formed via the programmable Watson–Crick base pairs (bps) between a bulged helix and a hairpin loop. Because both interacting parts are topologically closed, this motif exhibits a so-called paranemic cohesion[50,51] and allows the association of tiles without free ends. Therefore, each of the homooligomerizable tiles in this work was constructed from a single RNA strand. Through a series of straightforward variations, we demonstrate that a wide assortment of extended and finite-sized structures can be created, with their curvature, torsion and number of helices readily controlled. Further, we show that bKL-based tiles can be inserted into a tRNA scaffold for overexpression in bacterial cells, manifesting their promise for mass production and in vivo applications. Finally, we extend the utility of the bKL to other contexts by using it to position aptamers on RNA origami, and creating a DNA version of the motif.

Results and discussion

Design of the bKL motif. Design of the bKL was inspired by the RNA KL complex from the HIV-1 dimerization initiation site (DIS)[52]. This KL comprises two hairpins, binding to each other via Watson–Crick bps over a 6-nucleotide region within the hairpins' 9-nucleotide apical loops. The remaining three nucleotides in each loop are unpaired purines (here As); two reside on the 5′ side and one on the 3′ side of the kissing region so that the loop sequence is 2A-6N-1A. The two 5′ As, serving as a linker, return the strand from the kissing helix to the stem and span a distance of ~14 Å. We found that this distance can accommodate the replacement of the two-A linker with an RNA A-helix (Supplementary Fig. 1). This enabled design of the bKL through motif fusion (Fig. 1a,b), which turns one hairpin loop of the original KL into a bulge having the sequence of 6N-1A so that the Watson–Crick bps now form between a bulge and a hairpin loop (Fig. 1c). As with its parent KL, bKL's cohesion is paranemic.

We expected the bKL to retain the coaxial stacking present between the stems and kissing helix of the KL and, thus, to have a T shape. Therefore, it is reminiscent of the DNA T-junction[53], which involves cohesion between a bulged helix and a 5′ free end. Like the DNA T-junction, its branched geometry and rigidity (from coaxial stacking) make the bKL a versatile construction module. Meanwhile, similar to both RNA KLs and DNA T-junctions, the 6-bp Watson–Crick interaction of our bKL enables the programming of many specific binding interactions; by contrast, paranemic tetraloop/tetraloop-receptor interactions have quite limited programmability and specificity[54].

Multiple bKLs can be combined to create a single tile that self-assembles into higher-order structures. Figure 1d depicts how two bKLs can be incorporated into a Z-shaped tile (Z-tile) to specify the formation of a ladder-like structure (below termed 'ladder'). The two helical segments between hairpin loops and bulges are dubbed 'beams', and the helical segment between the two bulges a 'strut'. In the assembled ladder, extended coaxially stacked pseudo-continuous helices are termed 'rails'. Next, we show how to achieve geometric diversity by adjusting beam and strut length, or incorporating other motifs.

Control of torsion and symmetry. We began our study with simple Z-tiles having beams of equal length (x). The dihedral angle between adjacent Z-tiles (and hence ladder torsion) are determined by the twist contributed by each tile. To achieve a dihedral angle of zero, each repeat unit must be separated by an integral number of RNA turns (that is multiples of 11 bps) along the rails. For each bKL, we assumed that (as observed for KLs by NMR[55]) each unpaired 3′ A stacks between neighboring helices, adding a total of two bp equivalents (bp equiv.; in schematics we omit 3′ As for clarity). Therefore, we modelled each bKL as contributing a twist equivalent to that of an 8-bp helix and each tile an ($x+8$)-bp helix. Using this principle, we designed three Z-tiles (Fig. 2a): **LZB14** of minimal twist, and **LZB13** and **LZB15** of left- and right-handed twists, respectively.

Assembly of **LZB14** predominantly yielded ladders that closed into rings ranging from 40 to 130 nm in diameter (Fig. 2b,c and Supplementary Figs. 6 and 7), although ladders up to a micrometre long were occasionally observed (Fig. 2d). As expected, no evidence of twisting (for example periodic crossings of rails) was observed. The predominance of rings suggests that ladders were flexible and/or that the bKL has some intrinsic curvature: adjacent Z-tiles in a ladder are related by a translational symmetry, allowing the accumulation of any out-of-plane curvature caused by the bKL geometry. Introduction of torsion into **LZB13** and **LZB15** ladders provided one way to discourage ring formation. By atomic force microscopy (AFM; Fig. 2e,g and Supplementary Figs. 8 and 10), several micrometre-long filaments were observed for both tiles. Cryogenic electron microscopy (cryo-EM), on the other hand, provided a way to visualize structures in their native states, without the artefacts created by surface adsorption (Fig. 2f,h and Supplementary Figs. 9 and 11). We could observe a twist via periodic crossings of the rails, but could not determine the absolute handedness of ladders, as it is ambiguous in two-dimensional (2D) transmission electron microscopy and there was not enough contrast for tomography. Unlike with **LZB14**, small rings were rarely observed because ring closure requires the matching of the phase of ladder twist—thus the addition of torsion greatly decreases the probability that the two ends of the ladder will find each other in an orientation appropriate to bind.

Symmetry manipulation provides a second method to suppress the out-of-plane curvature observed in **LZB14** ladders. If every other tile in the ladder is flipped, bending from face-up tiles can cancel that from face-down ones (that is, so-called corrugated design[56]). To achieve this, we converted the Z-tile into a C-tile by changing the strut length (s) from an even number of helical half-turns to an odd number and accordingly designed **LCS16** ($s=16$) and **LCS27** ($s=27$; Fig. 2i). As expected, C-tiles assemble into ladders with both torsion and curvature minimized (Fig. 2j–m and Supplementary Figs. 12–15), although a few large (micrometre-scale) rings were also observed.

Interestingly, **LCS16** ladders sometimes associated laterally into wider structures under AFM (Fig. 2j and Supplementary Fig. 12), but not under cryo-EM (Fig. 2k and Supplementary Fig. 13). Base-stacking between blunt ends presents an opportunity for helices to stick together—this phenomenon has been used to programme the association of a variety of DNA nanostructures[28,29]. Thus, we suggest that sample preparation for dry AFM encourages ladders to associate via base-stacking between struts. For struts from different ladders to stack, the strut ends must be displaced from the position where they connect to the beams, implying a certain flexibility of the bKL (Supplementary Fig. 16). The occurrence of stacking between C-tile ladders, but not Z-tile ladders, is further evidence for the lack

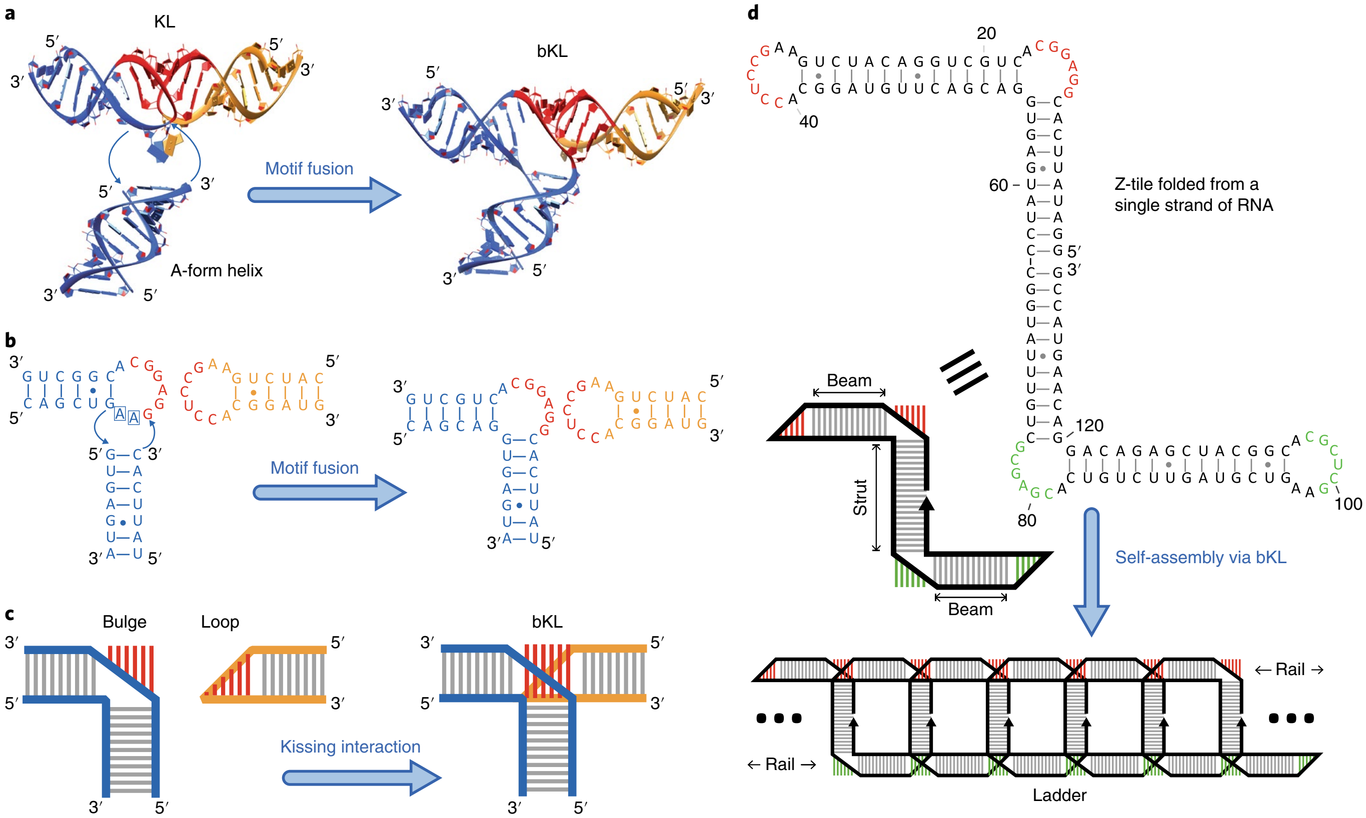

Fig. 1 | The bKL motif. a,**b**, Helical representation (**a**) and exemplary sequence details (**b**) of the motif fusion process used to design a bKL from a coaxially stacked linear KL and an A-form helix. The two hairpins of the KL bind via six Watson–Crick bps between red-coloured nucleotides in their loop regions; the remaining nucleotides of each hairpin (coloured blue at left and orange at right) include based-paired stems and three unpaired As. By replacing two of the unpaired As (boxed in **b**) in the left-hand hairpin with an A-form helix, the left-hand loop is converted into a bulge that can still base-pair with the loop of the right-hand hairpin. **c**, The formation of a bKL, coloured to match **a** and **b**. **d**, The use of bKLs to create a one-stranded Z-tile that self-assembles into a higher-order ladder. The nucleotides from the interacting bulges and hairpin loops are coloured the same (red or green).

of torsion and curvature in C-tile ladders—any significant bend or twist would disrupt the long-range alignment of struts, decreasing the opportunity for strut ends to match and stack.

Besides the flexibility that allows **LCS16** ladders to stack, the structures examined so far provide evidence for three additional types of intrinsic flexibility of the bKL (Supplementary Fig. 17): (1) out-of-plane bending of the beams, (2) rotational freedom of the strut along its axis and (3) in-plane bending of the beams. Below we harness the flexibility of the bKL to design a series of more complex structures.

Control of in-plane curvature. Closed annuli can be designed using Z-tiles having beams of different lengths ($x \neq y$), so that the binding of tiles forms trapezoidal repeat units and the resulting ladders bend towards the shorter trapezoid base. To achieve flat annuli, the bases of the trapezoid must further be chosen to be an integral number of helical turns. Two different Z-tiles with this property were designed (Fig. 3a). **RZB14/25**, whose beam lengths differ by one helical turn, sets the repeat length along the inner circle to two helical turns (22 bp) and that of the outer circle to three helical turns (33 bp). Geometrical analysis predicted that **RZB14/25** should form an unstrained planar annulus containing 16 or 17 tiles (Supplementary Fig. 18), having a diameter of 47 or 50 nm. **RZB14/36**, with a two-turn difference between trapezoid bases, was expected to form smaller annuli of greater curvature, containing 8 or 9 tiles and being 31 or 35 nm in diameter.

Experimentally, **RZB14/25** assembled into annuli of different sizes (Fig. 3b,c and Supplementary Figs. 19–21), potentially due to bKL flexibility and/or assembly kinetics (rates of intermolecular assembly versus intramolecular ring closure). To our surprise, **RZB14/36** formed two morphologically distinct structures (Fig. 3d and Supplementary Figs. 22 and 23). One was the expected smaller annulus; the other was a long linear filament, which appeared to be ~30% thicker (1.6–1.8 nm in height) than the annulus (1.2–1.3 nm in height), when examined using dry AFM (Supplementary Fig. 23). Based on the height of the unexpected filaments, we propose that they are, in fact, double-layered ladders, with three rails and a narrow, triangular cross-section (bottom right of Fig. 3a and Supplementary Figs. 24 and 25). If a purer sample of small annuli is desired, passage through a 0.22 μm filter removes most filaments, leaving annuli as the dominant species in the filtrate (Fig. 3e,f and Supplementary Figs. 26 and 27).

The formation of two different structures from **RZB14/36** suggested that the large in-plane curvature of 8-tile **RZB14/36** annuli might be near the bending limit that can be achieved with bKL-based Z-tiles. To investigate this limit, we designed **RZB14/47** to have a three-turn difference between beams (Supplementary Figs. 28 and 29). Indeed, instead of the small single-layered annuli, only larger double-layered annuli (formed similarly to the **RZB14/36** filaments, Supplementary Fig. 30) were observed.

Combining torsion and curvature. By incorporating both torsion and curvature into a tile, more complex 3D space curves can be achieved. Starting from **RZB14/25**, left- or right-handed torsion was introduced by simultaneously removing or adding one bp in both beams to produce tiles **RZB13/24** and **RZB15/26** (Fig. 3g). These two tiles were predicted to form helical ladders, which

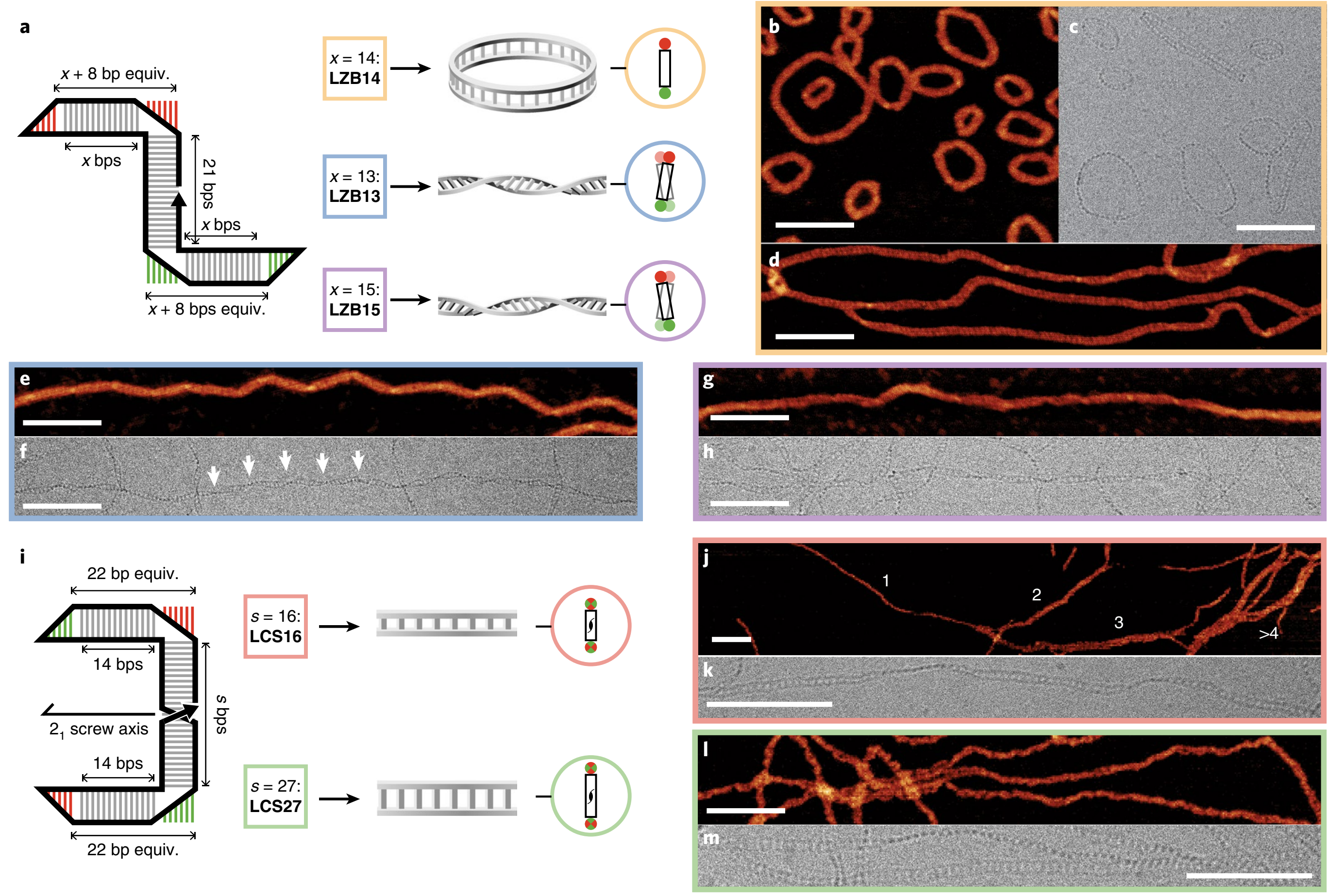

Fig. 2 | Effects of beam and strut lengths on ladders made from tiles with beams of equal length. a–h, Three Z-tiles of different beam length (x) and constant strut length ($s = 21$ bp ≈ 2 helical turns). Tile nomenclature is in Supplementary Fig. 2. Colour-coded boxes enclosing tile parameters match the colour of circles around cross-sections and outlines of image data. AFM images are colour; cryo-EM images are greyscale. **LZB14** has 14-bp beams so that the twist contributed by each tile is equivalent to 22 bp, an integral number of helical turns that minimizes torsion. Without torsion, Z-tile symmetry allows out-of-plane curvature to accumulate, resulting in mostly small rings (**b**,**c**) and a few larger structures (**d**) forming. By decreasing (**LZB13**) or increasing (**LZB15**) beam length by 1 bp, left- (**e**,**f**) and right-handed (**g**,**h**) twisted ladders were formed. Ladder twist measured by cryo-EM was 16–18 tiles per turn for **LZB13** and 17–21 tiles per turn for **LZB15**. Arrows in **f** indicate nodes between half-turns, used to measure ladder twist. Observed ladder twists were smaller than the maximum possible (11 tiles per turn) given the torsion created by adding or removing 1 bp per beam, suggesting some torsion was relaxed elsewhere. No superhelices were observed, so excess torsion may have been relaxed by bKL flexibility. **i–m**, Strut length of **LZB14** was changed from an even to an odd number of half-turns to create C-tiles **LCS16** (three half-turns) and **LCS27** (five half-turns). Corresponding ladders have both minimized torsion (via 14-bp beams) and minimized curvature (by a screw-axis symmetry). Wider filaments in **j** result from lateral stacking of ladders; numeric labels indicate number of ladders per filament. Scale bars, 100 nm.

we term ‘nano-ramens’ after their ramen-noodle-like appearance. Compared to the left-handed nano-ramens assembled from **RZB13/24** (Fig. 3h,i and Supplementary Figs. 31 and 32), right-handed **RZB15/26** nano-ramens appeared to be more flexible, as suggested by a curlier appearance and an increase in cyclic structures (Fig. 3j,k and Supplementary Figs. 33 and 34). The interplay of torsion, curvature and bKL flexibility makes it difficult to predict the helical parameters of nano-ramens. Experimentally, **RZB13/24** nano-ramens have a diameter of 16–20 nm and period of ~55 nm; **RZB15/26** structures have a wider diameter (20–30 nm) and longer (~60 nm) period.

Multi-railed ladders. Adding more rails to a ladder enables the creation of filaments that are stiffer, have different symmetries or bear more sites for functionalization. We explored two strategies to construct multi-railed ladders. The first employs Z-tiles with unequal beam lengths, so that each tile contributes an integral number of helical turns L along the longer beam, and a non-integer number of turns S (which approximately divides into L to yield an integer M) along the shorter beam (Fig. 4a). The resulting ladder has a central rail comprising the shorter beams, and M peripheral rails comprising the longer beams (spaced at intervals of $\theta = 360^\circ/X$ around the central rail, where X is the smallest integer so that SX is approximately an integer). According to this principle, we designed two Z-tiles—**LZB19/47** and **LZB10/47** (Fig. 4a)—to construct the three- (Fig. 4b,c and Supplementary Figs. 35 and 36) and four-railed ladders (Fig. 4d,e and Supplementary Figs. 37 and 38). This approach is similar to the unintended double-layered, three-railed ladder assembled from **RZB14/36**. However, for that structure ($L = 4$, $S = 2$, $M = 2$, $X = 1$, $\theta = 360^\circ$), were the tiles not flexible, the two long-repeat rails would be superimposed on each other, yielding a steric clash.

Our second strategy for creating multi-railed ladders was to generalize C-tiles to ‘claw-tiles’ by connecting n half-C-tiles via an n-way junction (nWJ) so that each claw-tile possesses n beams (Fig. 4f). A 3WJ was used to design branched tile **LCS3WJ**, which self-assembled cleanly into a three-railed ladder (Fig. 4g,h and

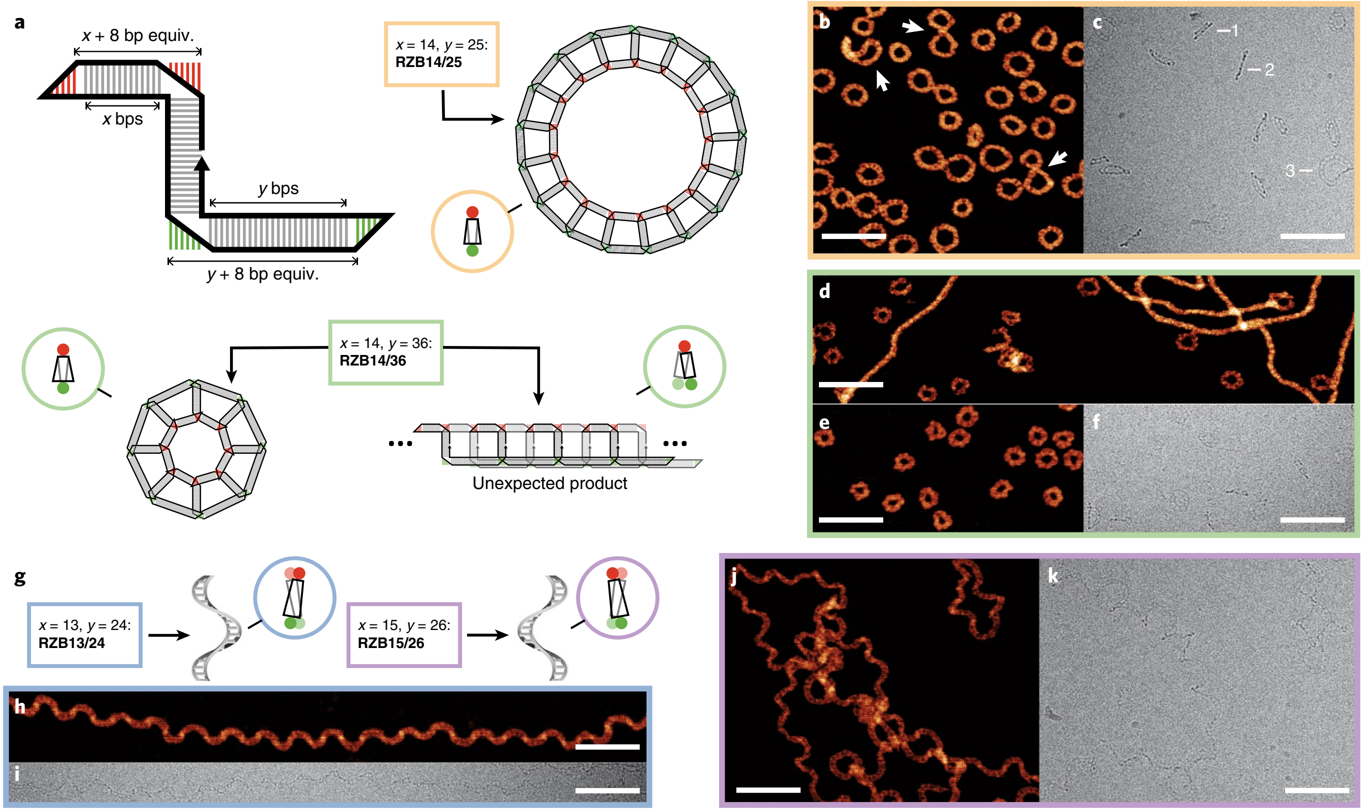

Fig. 3 | Controlling in-plane curvature using tiles of unequal beam lengths. a–f, Using tiles with beams of different lengths ($x \neq y$). Colour-coded boxes enclosing tile parameters match the colour of circles around cross-sections and outlines of image data. AFM images are colour; cryo-EM images are greyscale. **RZB14/25** ($y-x=11$ bps, that is, 1 turn) was predicted to form annuli 47–50 nm in diameter (16–17 tiles) and mostly assembled into 36–50 nm annuli. Annuli with fewer or greater than 15–18 tiles assumed non-planar geometries to release strain: those with fewer tiles, conical frustums, while those with more, saddle shapes (Supplementary Fig. 21). White arrows in AFM (**b**) show structures hypothesized to be large (up to 25-tile) non-planar shapes, which have collapsed on the surface. Numeric labels in cryo-EM (**c**) indicate different shapes: (1) frustum, (2) planar annulus and (3) saddle. **RZB14/36** ($y-x=22$ bps) was predicted to form 31–35 nm annuli (8 or 9 tiles) and assembled into 26–38 nm annuli (7–10 tiles) as well as unexpected, micrometre-long filaments for which we propose a three-railed structure (**a**, bottom right) wherein one edge of each filament is a single rail formed by the shorter beam of each tile and the other edge comprises two closely spaced rails, each formed by the longer beam of every other tile. The pairing of two short beams for each long beam yields a four-turn repeat unit without in-plane bending. Filaments could be mostly removed by filtering (**e**,**f**). **g**–**k**, Torsion and in-plane curvature combine to create helical nano-ramens in which the rails trace out a pair of Bertrand curves (space curves sharing normal lines; assuming bKLs are perfect T shapes, the strut provides a common normal to both rails). Designed using bp deletion and insertion on **RZB14/25**, tiles **RZB13/24** and **RZB15/26** form left-handed (**h**,**i**) and right-handed (**j**,**k**) nano-ramens, respectively. Scale bars, 100 nm.

Supplementary Figs. 39 and 40). Analogously, a four-railed ladder was self-assembled from tile **LCS4WJ** possessing a 4WJ (Fig. 4i,j and Supplementary Figs. 41 and 42). Unlike Z-tile-based multi-railed ladders, whose peripheral rails necessarily share the same sequence, claw-tile-based ladders provide the ability to break symmetry between rails and enable the uniquely addressable functionalization of each rail.

Out-of-plane curvature for 3D nanocages. The structures that we have so far described have no well-defined size: they were either extended ladders, or annuli with only somewhat tight size distributions. In the latter case, curvature was designed to specify annuli with an exact number of tiles, N, but because N was relatively large, tile insertion or omission required only a small deformation (per tile), which was easily accommodated by the tiles' flexibility. However, it is common for natural proteins to homooligomerize into finite assemblies containing a definite number of subunits. These natural systems normally exhibit a closed point-group symmetry that constrains the number of subunits arranged around a principal axis of rotation[2]. Using such a symmetry we designed tile **CZB12b11**, which preferentially forms a tetrameric nanocage (Fig. 5a). Beginning with a Z-tile, we introduced an out-of-plane bend into the midpoint of each beam by inserting a 90°-angle 5-nucleotide (AACUA) bulge from domain IIa of the internal ribosome entry site of the hepatitis C virus (HCV)[57]. Further, we arranged the pattern of bKL interactions (numeric labels in Fig. 5a) to render the tetramer D_2 symmetric. This ensured that only even-numbered N-mers having $D_{N/2}$ symmetry would be allowed and prevented the formation of C_3- and C_5-symmetric trimers and pentamers, which otherwise would be likely to form due to tile flexibility. The formation of dimers and hexamers, although allowed by symmetry, should be unlikely due to the requirement of greater flexibility and tile distortion.

Beyond theoretical considerations of geometry and symmetry, experimental salt concentrations can profoundly affect self-assembly: the formation of KL[20] and the folding of the RNA tertiary structure[58] are highly salt dependent. Therefore, we tested different annealing buffers to optimize nanocage assembly (Fig. 5b), and found that a buffer containing 100 mM Na^+ and 0.3 mM Mg^{2+} (Fig. 5b, lane 3) gave the desired product in an excellent (>95%) yield. AFM (Fig. 5c) and cryo-EM (Fig. 5d) revealed square-shaped particles of uniform size. The structural model obtained by cryo-EM

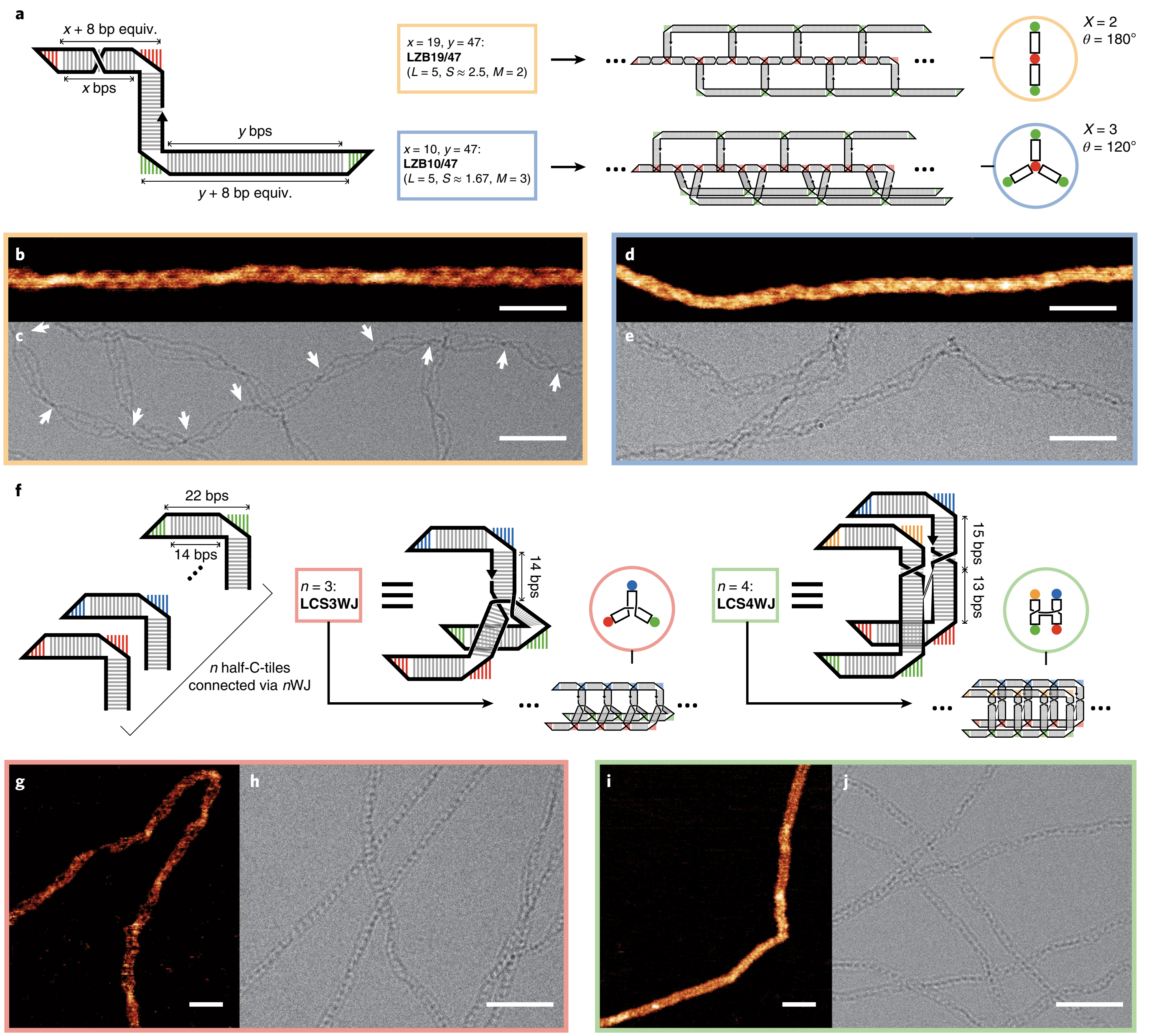

Fig. 4 | Two strategies to construct multi-railed ladders. a, Multi-railed ladders were assembled from Z-tiles with beams of unequal lengths. **LZB19/47** and **LZB10/47** were designed to create the three- and four-railed ladders, respectively. Colour-coded boxes enclosing tile parameters match the colour of circles around cross-sections and outlines of image data. **b**,**c**, Three-railed ladders assembled from **LZB19/47**. AFM images are colour; cryo-EM images are greyscale. Because the distances $2S = 54$ bps (along the central rail) and $L = 55$ bps (along a peripheral rail) differ by a single bp over a five-turn span, we expected a ladder twist with a period of 11 tiles or 169 nm. Measurements of the distances between visible nodes (indicated by white arrows in cryo-EM images) in the ladders gave a somewhat shorter period of 104 nm ± 18 nm ($N = 10$ half-periods) with roughly 7 tiles. **d**,**e**, Four-railed ladder assembled from **LZB10/47**. While the difference between distances $3S = 54$ bps and $L = 55$ bps predicts a significant twist for **RZB10/47** ladders, their three peripheral rails could not be easily differentiated in cryo-EM, making estimation of twist difficult. **f**, Claw-tiles were designed using an *n*WJ to connect *n* half-C-tiles. **LCS3WJ** and **LCS4WJ** were designed to create three- and four-railed ladders, respectively. **g**–**j**, Structures assembled from **LCS3WJ** (**g**,**h**) and **LCS4WJ** (**i**,**j**). Ladders assembled from **LCS3WJ** and **LCS4WJ** were expected to be of minimal twist; long straight filaments in cryo-EM images (**h**,**j**) support this prediction. Scale bars, 50 nm.

single-particle reconstruction (Fig. 5e,f) reveals that struts assume a tilt of ~10°, conferring an overall left-handed twist to the cage. Though a handful of RNA nanocages have been constructed using multiple tiles[36,37] or using a single tile formed from multiple RNA strands[59], ours is an example of the high-yield assembly of homooligomeric nanocages from only one strand of RNA.

Cotranscriptional assembly and cellular production. For all the structures described so far, tiles were first synthesized and purified from in vitro transcription, and then self-assembled via annealing. The fact that the intramolecular folding of the RNA secondary structure (10–100 μs) proceeds several orders of magnitude faster[60,61] than both the tiles' synthesis by RNA polymerase (~0.5 s at 200–400 nucleotides s^{-1}) and intermolecular assembly (half-life $t_{1/2} = 10$ s at 1 μM for the interacting parts of bKL, assuming bKL's association kinetics are similar to those of KL with an association rate constant k_a of 10^5 M^{-1} s^{-1} (ref. [62])) suggests that the assemblies should be able to form cotranscriptionally[22,49] while the tiles are being enzymatically

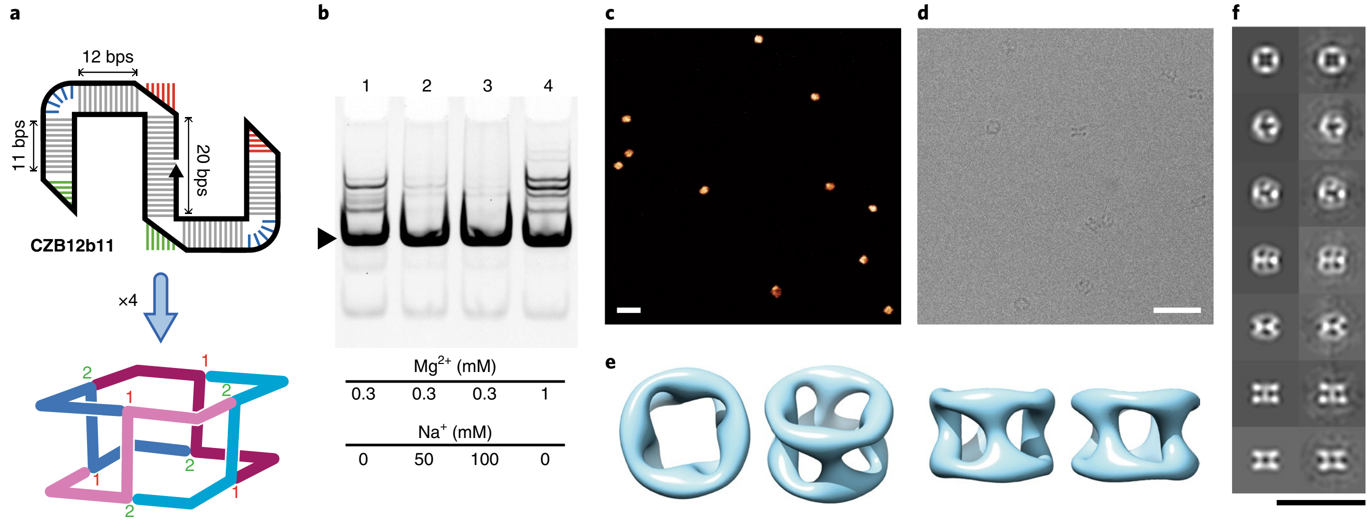

Fig. 5 | Tetrameric RNA nanocage. **a**, A 90°-angle AACUA bulge motif[57] (blue) was added to each beam of a Z-tile to create **CZB12b11**; this moved both hairpin loops out of the plane of the bulges to create a 3D geometry compatible with the formation of a tetrameric cage. Numbers indicate the identity of particular bKLs that result in D_2 symmetry. **b**, Native PAGE shows the salt concentrations explored to optimize the assembly yield of the tetramer (black triangle). **c**,**d**, AFM (**c**) and cryo-EM (**d**) images of the tetrameric nanocage. **e**, Structural model from cryo-EM single-particle reconstruction. **f**, Comparison of representative 2D projections of the 3D reconstruction (left) and corresponding class averages of individual particles (right). Full comparison is in Supplementary Fig. 43. Scale bars, 40 nm.

synthesized at a constant temperature of 37 °C. Therefore, we tested the cotranscriptional assembly of two representative Z-tiles, **LZB13** and **RZB14/25** (which, when annealed, form linear twisted ladders and annuli, respectively). Indeed, cotranscriptional assembly produces distributions of structures qualitatively similar to those formed with annealing (Supplementary Fig. 44). The successful isothermal cotranscriptional assembly of these tiles encouraged us to explore their expression and folding in the cells.

Figure 6 shows the gene that we constructed to express an RNA tile in bacterial cells. Its design involved addressing challenges not present for in vitro transcription. To enhance the in vivo RNA stability and to demonstrate the tile's correct folding, we combined a basic Z-tile (similar to **LZB13**) with two other RNA folds—a tRNA scaffold[63,64] and a Spinach aptamer[65]—to form a construct that we termed **TSSP** (a Z-tile within a tRNA scaffold bearing a Spinach aptamer) as shown in Fig. 6b,c. The unique fold of the tRNA scaffold enables the artificial RNA construct to be precisely processed by cellular enzymes and to escape cellular RNases, leading to a better stability and cellular accumulation. Spinach aptamer[65], which folds into an elongated conformation[66] and fluoresces only when binding its fluorophore 3,5-difluoro-4-hydroxybenzylidene imidazolinone (DFHBI), was fused to the anticodon stem of a tRNA[67] to connect to the strut of the Z-tile via a well-structured 3WJ (ref. [68]; from the Φ29 pRNA).

After transformation with a **TSSP**-expressing vector and treatment with DFHBI, *Escherichia coli* cells became highly fluorescent (Fig. 6d). Because the Spinach aptamer sequence bookends both the 5′ and 3′ ends of the Z-tile domain, fluorescence served as an indicator of the complete synthesis of both the Spinach and Z-tile domain. Moreover, this result also indicated that the Spinach aptamer could fold correctly in vivo when attached to a Z-tile domain. Further experiments confirmed the full-length synthesis of **TSSP** RNA and its competence for ladder assembly. Total cellular RNA was extracted and analysed by denaturing polyacrylamide gel electrophoresis (dPAGE), and a sharp band corresponding to full-length **TSSP** RNA (254 nucleotides long) was observed only for the cells transformed with the **TSSP**-expressing vector (Fig. 6e). Gel-purified **TSSP** RNA was then annealed in vitro and the expected long filaments were indeed assembled (Fig. 6f,g and Supplementary Figs. 45 and 46). Therefore, at least in the case of in vitro thermal annealing, the insertion of the Spinach/tRNA fusion does not disturb the formation of ladders. Given the above lines of evidence, the correct in vivo folding of the **TSSP** tile and even the in vivo formation of ladders are very likely, but definitive proof may require either gentle, nondenaturing extraction of the ladders (which is likely to be more challenging than the extraction of the smaller RNA structures previously produced in vivo[69]), or high-resolution cryo-EM tomography of thin bacterial cells[70]. Nonetheless, the tRNA scaffold overexpression approach is appropriate for the biological mass production of bKL-based RNA tiles.

The bKL in RNA origami. A recently reported cotranscriptionally foldable RNA architecture—RNA origami[22]—derives its generality from the use of intramolecular 180° KLs and antiparallel 4WJs to organize RNA helices into parallel arrays. The paranemic cohesion provided by the KLs enables large RNA origami to be crafted from a single long strand. A major goal of RNA nanoarchitectures is to scaffold patterns of proteins and small molecules via RNA protein-binding motifs or aptamers[71]. Yet the first version of RNA origami left unclear how functional RNA motifs could be introduced at arbitrary positions within a structure. Grafting 3WJs into helices provides one possibility, but the presence of crucial KLs makes this impossible for a large number of positions and orientations. The bKL provides a perfect solution to this problem: by introducing a geometrically well-defined branch exactly at the point of paranemic cohesion, the bKL enables the insertion of a functional motif without compromising the structural integrity of an RNA helix. Figure 7a demonstrates this principle in the case of the simplest RNA origami structure, a two-helix tile (**DAE-bKL**), designed to assemble into hexagonal lattices (Fig. 7b) via intramolecular 120° KLs. Replacement of a conventional KL with a bKL allows the precise positioning and orientation of a protein-binding aptamer[72] (F6, binding the MS2 viral coat protein) while maintaining the rigidity of the tile and its assembly into a lattice. Liquid AFM (Fig. 7c and Supplementary Fig. 47) confirms the intended orientation of F6 aptamers, with three copies pointing inwards within each hexagonal cavity.

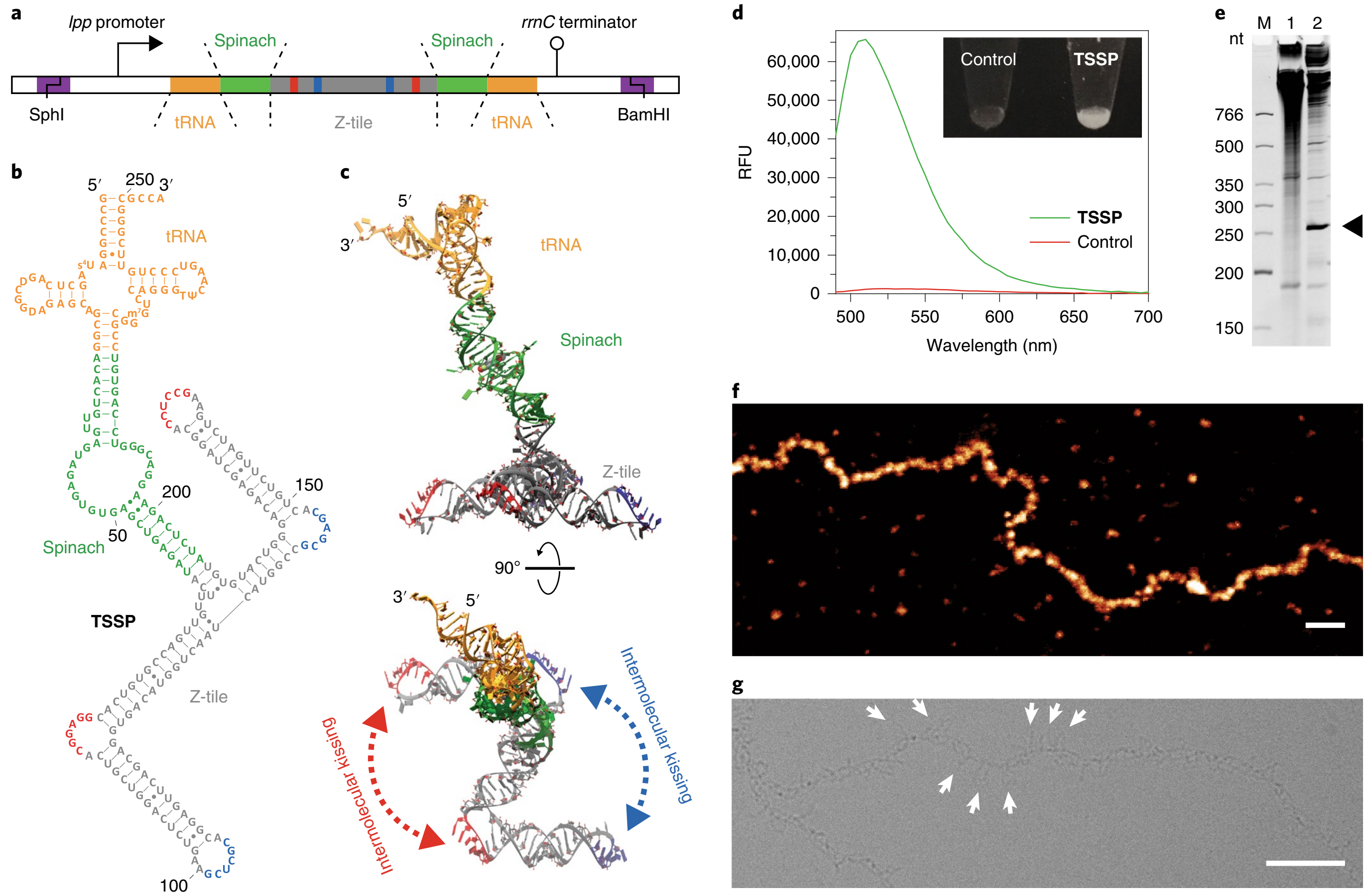

Fig. 6 | Cellular production of RNA tiles. a, Design of a gene encoding **TSSP**, a fusion of a tRNA scaffold (orange), a Spinach aptamer (green) and a Z-tile analogous to **LZB13** (grey with red and blue segments indicating bKL sequences) except that its bKL sequences were chosen so that every other tile is rotated by 180° in plane. **TSSP** was inserted between the SphI and BamHI sites of plasmid pUC19 for expression in *E. coli* under control of the *lpp* promoter and *rrnC* terminator. **b**, Predicted secondary structure of **TSSP**. **c**, Two views of a 3D model built from three known structures: a tRNA (Protein Data Bank ID: 1FIR)[67], the Spinach aptamer (4KZD)[66] and the Φ29 pRNA 3WJ (4KZ2)[68]. **d**, Emission spectra of bacterial cells with (**TSSP**) and without (control) transformation of the plasmid expressing **TSSP** in the presence of the Spinach fluorophore DFHBI under 469 nm excitation. RFU, relative fluorescence unit. Inset: photograph under UV excitation with SYBR Green emission filter. **e**, Denaturing PAGE of the total RNA extracted from bacterial cells without (lane 1) and with (lane 2) **TSSP**-expressing plasmid. A black triangle marks the **TSSP** band (254 nucleotides, nt). Lane M, DNA size marker. **f**,**g**, AFM (**f**) and cryo-EM (**g**) images of structures assembled from cell-produced, gel-purified **TSSP** via in vitro annealing. Spinach/tRNA fusions can be directly observed by cryo-EM (white arrows in **g**) and give **TSSP** ladders a brush-like appearance. Scale bars, 100 nm.

DNA version of the bKL motif. Paranemic DNA motifs are less developed, essentially limited to the large and complex PX motif that joins two helices side-by-side[50]. Direct adaptation of HIV-1 DIS KL (with its 2A-6N-1A sequence) to DNA was previously reported, but this KL adopts a 'peculiar' configuration[73] that does not generalize to other sequences. Thus, it is of interest to expand the vocabulary of DNA paranemic motifs. By considering the differences between A-form RNA and B-form DNA helices, we have been able to adapt the bKL from RNA to DNA with only minor modifications (Fig. 7d). As in the case of RNA bKL, we fused an extra helix to one hairpin loop to create a branch; paranemic cohesion was again provided by Watson–Crick bps between a 6-nucleotide bulge (with a sequence of 6N) and a 6-nucleotide region of a 9-nucleotide hairpin loop (with a sequence of 3A-6N). For the DNA bKL, the three unpaired nucleotides (dAs) in the loop are all positioned on the 5′ side of the kissing region and serve as a linker to return the strand from the kissing region to the stem across the major groove because the major groove of B-DNA (22 Å) is wider than that of A-RNA (16 Å). Assuming coaxial stacking similar to that in an RNA bKL, we modelled the DNA bKL as contributing the same twist as a standard 6-bp B-form DNA helix. Accordingly, a one-stranded C-tile containing two 15-bp beams (**dLCB15**) was designed (Fig. 7e) and assembled into a ladder having no apparent twist (Fig. 7f and Supplementary Fig. 48).

Conclusions

Though artificially designed via motif fusion, our 6-bp bKL closely resembles a number of naturally occurring bulge–loop kissing interactions in biological RNAs. Prominently, a 4-bp bKL formed by the Φ29 pRNA[74] has been used to construct various synthetic structures[37–39,69]. However, its short length is a potential disadvantage compared to the 6-bp bKL, both thermodynamically (having a smaller binding energy) and combinatorially (supporting an order of magnitude fewer orthogonal binding interactions). Besides naturally occurring bKLs, in vitro selection has generated aptamers that form bKLs with hairpin loops in HCV mRNA[75,76]. Natural and selected bKLs suggest that there is a huge space of bKLs, with different properties, left to be studied. For instance, both the number and position of unpaired nucleotides within the bulge and loop should profoundly impact tile flexibility and interhelical angle. Similarly, the number and sequence of bps within the kissing helix will dictate the thermodynamics and kinetics of bKL interactions.

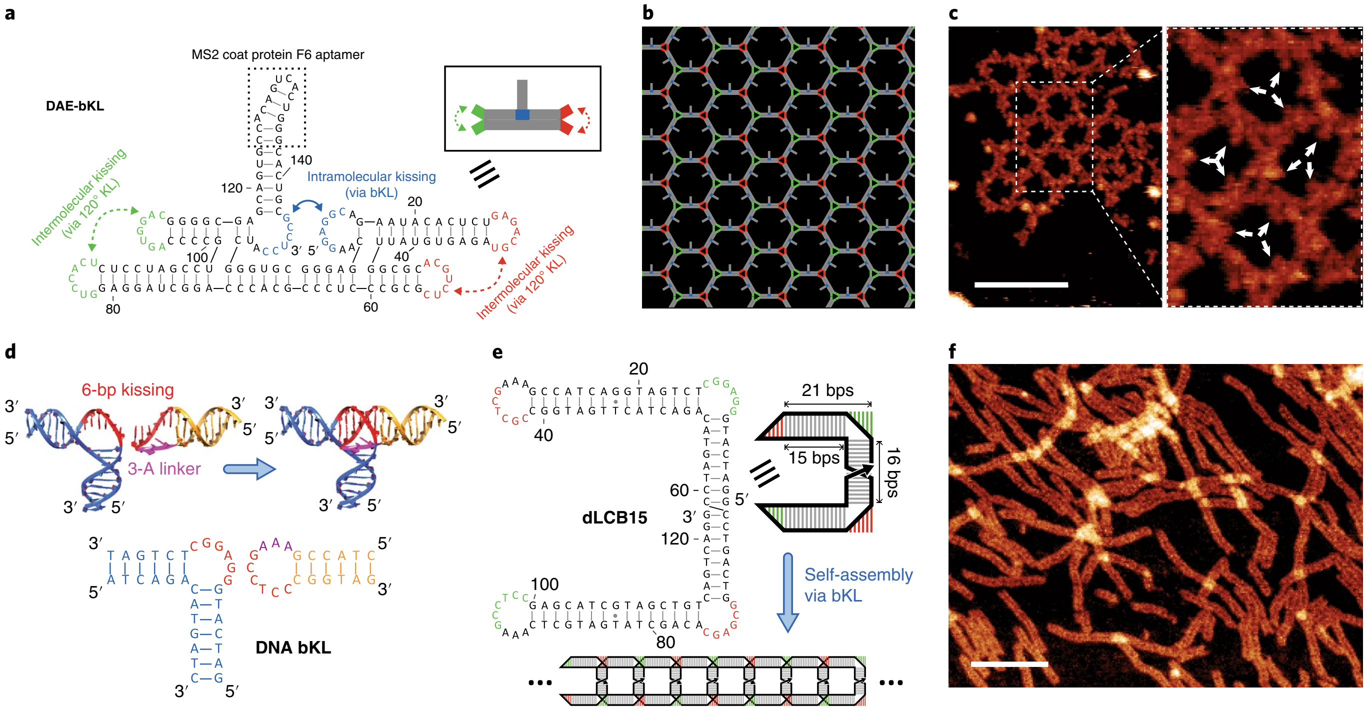

Fig. 7 | Integration of RNA bKLs into RNA origami tiles, and design of a DNA bKL. a, **DAE-bKL** was designed by the insertion of a bKL into a two-helix RNA origami tile (**2H-AE**[22] modified to be one turn narrower) to display the aptamer F6[72] (enclosed by a dashed box). Green and red sequences denote loops that form 7-bp intermolecular 120° KLs. **b**, The 2D lattice predicted to form from **DAE-bKL**. **c**, Liquid AFM of lattice cotranscriptionally assembled from **DAE-bKL**. White arrows show positions of F6 aptamers, pointed into each hexagonal cavity. Scale bar, 50 nm. **d**, DNA bKL formed by motif fusion. **e**, C-tile **dLCB15** designed using the DNA bKL motif, with a symmetry that minimizes curvature. G/T mismatches derive from an analogous RNA tile sequence. **f**, AFM of design from **e** reveals straight ladders. Scale bar, 100 nm.

Moreover, practical biomedical applications will require a systematic investigation of the physicochemical properties of bKL-based structures (for example in vivo stability, recently measured for RNA KL-based fibres[49]).

With respect to existing practices in DNA and RNA nanotechnology, we expect that bKLs will have important implications at the architectural level. Above, we demonstrated bKLs as a method for introducing a branch to augment RNA origami tiles with an aptamer. More generally, the bKL will provide an alternative for branching RNA and DNA structures into the third dimension, especially in large ssRNA and ssDNA origami[35]. Currently, branches in ssRNA and ssDNA origami are mediated by multi-WJs, which often restrict the complexity of strand paths (that is, the routing of the single strand through a structure) that can be designed without introducing topological problems and concomitant kinetic traps. Use of bKLs will greatly increase the number of available strand paths and enable designs that achieve more local folding and consequently higher yields.

The goal of this work was to explore the structural diversity enabled by homooligomerization of bKL-based tiles. However, still higher structural complexity could be realized by a system comprising many different tiles, similar to that achieved using DNA bricks[77,78]. One interesting application of such multi-tile systems would be to construct arbitrary space curves. Current approaches to curvature and torsion in 2D (ref. [79]) and 3D (refs. [80,81]) DNA origami work by changing the number of bps between crossovers to produce a deviation from the periodicity of an ideal B-form helix; desired curvature and torsion are generated by tuning the release and balancing of strain. Similar principles will also hold for bKL-based tiles, but recalibration will be required to account for the replacement of crossovers with struts. We envision that a library of bKL-based tiles of known curvature and torsion could be built, so that arbitrary space curves could be readily designed and assembled in a modular fashion. Multi-tile systems also enable control over assembly size. Perfect size control is straightforward for designs in which each tile appears only once at a unique position[77,78], but this approach is expensive. For the types of linear systems presented here, whose assembly is best modelled by step-growth polymerization[82], effective control of size distribution can be realized using inexpensive two-tile systems by adjusting the ratio of two bifunctional monomers, or adding a monofunctional cap (Supplementary Fig. 49). Overall, our explorations of the bKL motif have barely scratched the surface of what it could enable—we anticipate that it will open up entirely new avenues for the engineering of nucleic acids.

Methods

RNA sequence design and preparation. Sequences were designed via sequence symmetry minimization[83] using CANADA[84] and verified by Mfold[85] to ensure that each designed RNA folds into the desired secondary structure (see Supplementary Figs. 2–5 for sequences and predicted secondary structures, prepared with the assistance of VARNA[86]). Corresponding DNA template sequences are listed in Supplementary Tables 1 and 2. For all tiles except **DAE-bKL**, the first two nucleotides of reverse PCR primers were modified with a 2′-OMe group to reduce the 3′ transcriptional heterogeneity[87]. RNAs were synthesized by in vitro transcription using the HiScribe T7 High Yield RNA Synthesis Kit (NEB) with the corresponding DNA templates generated by PCR amplification of the gBlocks fragments (IDT) using the Q5 Hot Start High-Fidelity DNA Polymerase (NEB). Except where cotranscriptionally folded, RNAs were purified by dPAGE, ethanol precipitated and suspended in pure water.

RNA nanostructure assembly. Before assembly, RNAs were denatured at 90 °C for 1 min and snap-cooled on ice. For the assembly, unless stated otherwise, RNAs were diluted to 600 nM in ×1 TAE–Mg buffer (11 mM $MgCl_2$, 40 mM Tris, 20 mM acetic acid and 1 mM EDTA at pH 8.0) and annealed from 70 °C to 4 °C in three stages: 70 °C to 50 °C over 6 min, 50 °C to 37 °C over 20 min and 37 °C to 4 °C over 2 h.

For **CZB12b11** nanocages, buffer composition was optimized by varying the ratios of ×10 TAE–Mg buffer and 1 M NaCl, and yield was maximized at 0.3 mM Mg^{2+} and 100 mM Na^+ as estimated by 4% native PAGE (in ×0.5 TBE buffer supplemented by 3 mM of $MgCl_2$, ice-bath cooled).

Cellular production and fluorescence characterization of TSSP. The gene expressing **TSSP** (Supplementary Table 3) was cloned into the BamHI + SphI restriction sites of vector pUC19 and transformed into DH5α competent cells. Cells were grown overnight in fresh lysogeny broth medium containing 50 µg ml^{-1} ampicillin at 37 °C to an optical density measured at a wavelength of 600 nm (OD_{600nm}) of ~0.6–0.8. Total RNA was prepared by phenol/chloroform/isoamyl alcohol extraction. For in vitro assembly, **TSSP** RNA was purified by dPAGE. Fluorescence characterization was performed on intact bacterial cells in the presence of 20 µM DFHBI, synthesized according to a published method[65], with spectroscopy obtained by a Synergy H4 Hybrid Microplate Reader (BioTek) and photography obtained in the darkroom of an EC3 bioimaging system (UVP).

DNA preparation. Tile **dLCB15** was synthesized via splinted DNA ligation from two precursor strands by hybridization with a splint strand (Supplementary Table 4) using T4 DNA ligase (NEB). The full-length DNA was purified by dPAGE, and refolded via annealing similar to the RNA tiles.

AFM imaging. If not specified otherwise, AFM images were obtained by the dry mode due to its convenience and the smaller amount of damage caused by the probe tips. However, liquid AFM provides better resolution and was used to obtain Fig. 7c and Supplementary Figs. 25 and 28. Sample preparation for dry AFM was as follows: (1) we diluted the annealing mixtures ten times with ×1 TAE–Mg buffer, (2) deposited 5 µl onto a freshly cleaved mica (Ted Pella) to adsorb for 1 min, (3) dried the specimen with compressed air, (4) rinsed it with 20 µl of 2 mM $Mg(OAc)_2$ and (5) dried the specimen with compressed air again. Images were acquired on a Multimode 8 AFM in the 'ScanAsyst in Air' mode using ScanAsyst-Air probes (Bruker). For liquid AFM, sample preparation was similar to that of dry AFM except that, after sample deposition, 30 µl of imaging buffer (10 mM $NiCl_2$ and 10 mM Tris–HCl at pH 8.0) was added onto the mica. Images were obtained in liquid tapping mode using tip A of SNL-10 probes (Bruker). Based on the stability study of a model heterodimer system (Supplementary Fig. 50), all structures are expected to be stable at room temperature, at which AFM sample preparation and imaging were performed. Images were processed and prepared with Gwyddion.

Cryo-EM imaging and single-particle reconstruction. For all structures except the **CZB12b11** nanocages, the annealing mixture containing 600 nM RNA tiles was directly used for grid preparation. For the **CZB12b11** nanocages, the mixture was concentrated ten times with an Amicon Ultra centrifugal filter (molecular weight cut-off, 30 kDa). Next, 3 µl of solution was applied onto a glow-discharged C-flat holey carbon grid (product CF-1.2/1.3-4C; EMS), blotted for 5.5 s and immediately flash frozen by liquid-nitrogen-cooled liquid ethane with a Cryoplunge 3 System (GATAN). Images were collected on a JEOL 3200FS transmission electron microscope (300 kV) equipped with a K2 Summit camera (GATAN) under low-dose mode. For the structures without single-particle reconstruction, images were recorded at ×12,000 or ×25,000 microscope magnification with the defocus ranging from about −3.0 to −5.0 µm. For single-particle reconstruction of **CZB12b11** nanocages, images were recorded at ×25,000 microscope magnification with the defocus ranging from about −1.0 to −4.0 µm.

Single-particle reconstruction was performed using EMAN2[88], and 598 particles were used to generate reference-free class averages to build the initial model. Refinement was conducted with the full set of 1,440 particles. Resolution of the resulting density map was estimated to be 18.1 Å using the gold-standard FSC = 0.143 criterion, without applying any mask. The reconstructed model was visualized by UCSF Chimera[89].

Online content

Any Nature Research reporting summaries, source data, extended data, supplementary information, acknowledgements, peer review information; details of author contributions and competing interests; and statements of data and code availability are available at https://doi.org/10.1038/s41557-019-0406-7.

Received: 25 February 2019; Accepted: 6 December 2019;
Published online: 20 January 2020

References

1. Labeit, S. & Kolmerer, B. Titins: giant proteins in charge of muscle ultrastructure and elasticity. *Science* **270**, 293–296 (1995).
2. Goodsell, D. S. & Olson, A. J. Structural symmetry and protein function. *Annu. Rev. Biophys. Biomol. Struct.* **29**, 105–153 (2000).
3. Ali, M. H. & Imperiali, B. Protein oligomerization: how and why. *Bioorg. Med. Chem.* **13**, 5013–5020 (2005).
4. Pieters, B. J., van Eldijk, M. B., Nolte, R. J. & Mecinovic, J. Natural supramolecular protein assemblies. *Chem. Soc. Rev.* **45**, 24–39 (2016).
5. Desai, A. & Mitchison, T. J. Microtubule polymerization dynamics. *Annu. Rev. Cell Dev. Biol.* **13**, 83–117 (1997).
6. Bugyi, B. & Carlier, M. F. Control of actin filament treadmilling in cell motility. *Annu. Rev. Biophys.* **39**, 449–470 (2010).
7. Mitchison, T. J. & Cramer, L. P. Actin-based cell motility and cell locomotion. *Cell* **84**, 371–379 (1996).
8. Seeman, N. C. Nanomaterials based on DNA. *Annu. Rev. Biochem.* **79**, 65–87 (2010).
9. Zhang, F., Nangreave, J., Liu, Y. & Yan, H. Structural DNA nanotechnology: state of the art and future perspective. *J. Am. Chem. Soc.* **136**, 11198–11211 (2014).
10. Seeman, N. C. *Structural DNA Nanotechnology* (Cambridge Univ. Press, 2016).
11. Guo, P. The emerging field of RNA nanotechnology. *Nat. Nanotechnol.* **5**, 833–842 (2010).
12. Paillart, J. C., Marquet, R., Skripkin, E., Ehresmann, C. & Ehresmann, B. Dimerization of retroviral genomic RNAs: structural and functional implications. *Biochimie* **78**, 639–653 (1996).
13. Hill, A. C., Bartley, L. E. & Schroeder, S. J. Prohead RNA: a noncoding viral RNA of novel structure and function. *Wiley Interdiscip. Rev. RNA* **7**, 428–437 (2016).
14. Winfree, E., Liu, F., Wenzler, L. A. & Seeman, N. C. Design and self-assembly of two-dimensional DNA crystals. *Nature* **394**, 539–544 (1998).
15. Rothemund, P. W. et al. Design and characterization of programmable DNA nanotubes. *J. Am. Chem. Soc.* **126**, 16344–16352 (2004).
16. Stewart, J. M., Subramanian, H. K. K. & Franco, E. Self-assembly of multi-stranded RNA motifs into lattices and tubular structures. *Nucleic Acids Res.* **45**, 5449–5457 (2017).
17. Liu, H., Chen, Y., He, Y., Ribbe, A. E. & Mao, C. Approaching the limit: can one DNA oligonucleotide assemble into large nanostructures? *Angew. Chem. Int. Ed.* **45**, 1942–1945 (2006).
18. Tian, C. et al. Approaching the limit: can one DNA strand assemble into defined nanostructures? *Langmuir* **30**, 5859–5862 (2014).
19. Li, M., Zuo, H., Yu, J., Zhao, X. & Mao, C. One DNA strand homo-polymerizes into defined nanostructures. *Nanoscale* **9**, 10601–10605 (2017).
20. Horiya, S. et al. RNA LEGO: magnesium-dependent formation of specific RNA assemblies through kissing interactions. *Chem. Biol.* **10**, 645–654 (2003).
21. Nasalean, L., Baudrey, S., Leontis, N. B. & Jaeger, L. Controlling RNA self-assembly to form filaments. *Nucleic Acids Res.* **34**, 1381–1392 (2006).
22. Geary, C., Rothemund, P. W. & Andersen, E. S. RNA nanostructures. A single-stranded architecture for cotranscriptional folding of RNA nanostructures. *Science* **345**, 799–804 (2014).
23. Praetorius, F. et al. Biotechnological mass production of DNA origami. *Nature* **552**, 84–87 (2017).
24. Ducani, C., Kaul, C., Moche, M., Shih, W. M. & Hogberg, B. Enzymatic production of 'monoclonal stoichiometric' single-stranded DNA oligonucleotides. *Nat. Methods* **10**, 647–652 (2013).
25. Heiat, M., Ranjbar, R., Latifi, A. M., Rasaee, M. J. & Farnoosh, G. Essential strategies to optimize asymmetric PCR conditions as a reliable method to generate large amount of ssDNA aptamers. *Biotechnol. Appl. Biochem.* **64**, 541–548 (2017).
26. Veneziano, R. et al. In vitro synthesis of gene-length single-stranded DNA. *Sci. Rep.* **8**, 6548 (2018).
27. Chen, G. et al. Enzymatic synthesis of periodic DNA nanoribbons for intracellular pH sensing and gene silencing. *J. Am. Chem. Soc.* **137**, 3844–3851 (2015).
28. Woo, S. & Rothemund, P. W. Programmable molecular recognition based on the geometry of DNA nanostructures. *Nat. Chem.* **3**, 620–627 (2011).
29. Gerling, T., Wagenbauer, K. F., Neuner, A. M. & Dietz, H. Dynamic DNA devices and assemblies formed by shape-complementary, non-base pairing 3D components. *Science* **347**, 1446–1452 (2015).
30. Jasinski, D., Haque, F., Binzel, D. W. & Guo, P. Advancement of the emerging field of RNA nanotechnology. *ACS Nano* **11**, 1142–1164 (2017).
31. Wang, H., Di Gate, R. J. & Seeman, N. C. An RNA topoisomerase. *Proc. Natl Acad. Sci. USA* **93**, 9477–9482 (1996).
32. Liu, D. et al. Synthesizing topological structures containing RNA. *Nat. Commun.* **8**, 14936 (2017).
33. Afonin, K. A. et al. In vitro assembly of cubic RNA-based scaffolds designed in silico. *Nat. Nanotechnol.* **5**, 676–682 (2010).
34. Endo, M., Takeuchi, Y., Emura, T., Hidaka, K. & Sugiyama, H. Preparation of chemically modified RNA origami nanostructures. *Chem. Eur. J.* **20**, 15330–15333 (2014).
35. Han, D. et al. Single-stranded DNA and RNA origami. *Science* **358**, eaao2648 (2017).
36. Severcan, I. et al. A polyhedron made of tRNAs. *Nat. Chem.* **2**, 772–779 (2010).

37. Hao, C. et al. Construction of RNA nanocages by re-engineering the packaging RNA of Phi29 bacteriophage. *Nat. Commun.* **5**, 3890 (2014).
38. Shu, D., Moll, W. D., Deng, Z., Mao, C. & Guo, P. Bottom-up sssembly of RNA arrays and superstructures as potential parts in nanotechnology. *Nano Lett.* **4**, 1717–1723 (2004).
39. Shu, D., Huang, L. P., Hoeprich, S. & Guo, P. Construction of phi29 DNA-packaging RNA monomers, dimers, and trimers with variable sizes and shapes as potential parts for nanodevices. *J. Nanosci. Nanotechnol.* **3**, 295–302 (2003).
40. Dibrov, S. M., McLean, J., Parsons, J. & Hermann, T. Self-assembling RNA square. *Proc. Natl Acad. Sci. USA* **108**, 6405–6408 (2011).
41. Boerneke, M. A., Dibrov, S. M. & Hermann, T. Crystal-structure-guided design of self-assembling RNA nanotriangles. *Angew. Chem. Int. Ed.* **55**, 4097–4100 (2016).
42. Ohno, H. et al. Synthetic RNA-protein complex shaped like an equilateral triangle. *Nat. Nanotechnol.* **6**, 116–120 (2011).
43. Khisamutdinov, E. F. et al. Enhancing immunomodulation on innate immunity by shape transition among RNA triangle, square and pentagon nanovehicles. *Nucleic Acids Res.* **42**, 9996–10004 (2014).
44. Chworos, A. et al. Building programmable jigsaw puzzles with RNA. *Science* **306**, 2068–2072 (2004).
45. Jaeger, L. & Chworos, A. The architectonics of programmable RNA and DNA nanostructures. *Curr. Opin. Struct. Biol.* **16**, 531–543 (2006).
46. Grabow, W. W. & Jaeger, L. RNA self-assembly and RNA nanotechnology. *Acc. Chem. Res.* **47**, 1871–1880 (2014).
47. Geary, C., Chworos, A., Verzemnieks, E., Voss, N. R. & Jaeger, L. Composing RNA nanostructures from a syntax of RNA structural modules. *Nano Lett.* **17**, 7095–7101 (2017).
48. Grabow, W. W. et al. Self-assembling RNA nanorings based on RNAI/II inverse kissing complexes. *Nano Lett.* **11**, 878–887 (2011).
49. Rackley, L. et al. RNA fibers as optimized nanoscaffolds for siRNA coordination and reduced immunological recognition. *Adv. Funct. Mater.* **28**, 1805959 (2018).
50. Zhang, X., Yan, H., Shen, Z. & Seeman, N. C. Paranemic cohesion of topologically-closed DNA molecules. *J. Am. Chem. Soc.* **124**, 12940–12941 (2002).
51. Afonin, K. A., Cieply, D. J. & Leontis, N. B. Specific RNA self-assembly with minimal paranemic motifs. *J. Am. Chem. Soc.* **130**, 93–102 (2008).
52. Ennifar, E., Walter, P., Ehresmann, B., Ehresmann, C. & Dumas, P. Crystal structures of coaxially stacked kissing complexes of the HIV-1 RNA dimerization initiation site. *Nat. Struct. Biol.* **8**, 1064–1068 (2001).
53. Hamada, S. & Murata, S. Substrate-assisted assembly of interconnected single-duplex DNA nanostructures. *Angew. Chem. Int. Ed.* **48**, 6820–6823 (2009).
54. Fiore, J. L. & Nesbitt, D. J. An RNA folding motif: GNRA tetraloop-receptor interactions. *Q. Rev. Biophys.* **46**, 223–264 (2013).
55. Kieken, F., Paquet, F., Brule, F., Paoletti, J. & Lancelot, G. A new NMR solution structure of the SL1 HIV-1Lai loop-loop dimer. *Nucleic Acids Res.* **34**, 343–352 (2006).
56. Yan, H., Park, S. H., Finkelstein, G., Reif, J. H. & LaBean, T. H. DNA-templated self-assembly of protein arrays and highly conductive nanowires. *Science* **301**, 1882–1884 (2003).
57. Dibrov, S. M., Johnston-Cox, H., Weng, Y. H. & Hermann, T. Functional architecture of HCV IRES domain II stabilized by divalent metal ions in the crystal and in solution. *Angew. Chem. Int. Ed.* **46**, 226–229 (2007).
58. Woodson, S. A. Metal ions and RNA folding: a highly charged topic with a dynamic future. *Curr. Opin. Chem. Biol.* **9**, 104–109 (2005).
59. Yu, J., Liu, Z., Jiang, W., Wang, G. & Mao, C. De novo design of an RNA tile that self-assembles into a homo-octameric nanoprism. *Nat. Commun.* **6**, 5724 (2015).
60. Heilman-Miller, S. L. Effect of transcription on folding of the *Tetrahymena* ribozyme. *RNA* **9**, 722–733 (2003).
61. Cruz, J. A. & Westhof, E. The dynamic landscapes of RNA architecture. *Cell* **136**, 604–609 (2009).
62. Rist, M. & Marino, J. Association of an RNA kissing complex analyzed using 2-aminopurine fluorescence. *Nucleic Acids Res.* **29**, 2401–2408 (2001).
63. Ponchon, L. & Dardel, F. Recombinant RNA technology: the tRNA scaffold. *Nat. Methods* **4**, 571–576 (2007).
64. Ponchon, L., Beauvais, G., Nonin-Lecomte, S. & Dardel, F. A generic protocol for the expression and purification of recombinant RNA in *Escherichia coli* using a tRNA scaffold. *Nat. Protoc.* **4**, 947–959 (2009).
65. Paige, J. S., Wu, K. Y. & Jaffrey, S. R. RNA mimics of green fluorescent protein. *Science* **333**, 642–646 (2011).
66. Huang, H. et al. A G-quadruplex-containing RNA activates fluorescence in a GFP-like fluorophore. *Nat. Chem. Biol.* **10**, 686–691 (2014).
67. Bénas, P. et al. The crystal structure of HIV reverse-transcription primer tRNA(Lys,3) shows a canonical anticodon loop. *RNA* **6**, 1347–1355 (2000).
68. Zhang, H. et al. Crystal structure of 3WJ core revealing divalent ion-promoted thermostability and assembly of the Phi29 hexameric motor pRNA. *RNA* **19**, 1226–1237 (2013).
69. Li, M. et al. In vivo production of RNA nanostructures via programmed folding of single-stranded RNAs. *Nat. Commun.* **9**, 2196 (2018).
70. Dobro, M. J. et al. Uncharacterized bacterial structures revealed by electron cryotomography. *J. Bacteriol.* **199**, e00100-17 (2019).
71. Delebecque, C. J., Lindner, A. B., Silver, P. A. & Aldaye, F. A. Organization of intracellular reactions with rationally designed RNA assemblies. *Science* **333**, 470–474 (2011).
72. Convery, M. A. et al. Crystal structure of an RNA aptamer–protein complex at 2.8 Å resolution. *Nat. Struct. Biol.* **5**, 133–139 (1998).
73. Barbault, F., Huynh-Dinh, T., Paoletti, J. & Lanceloti, G. A new peculiar DNA structure: NMR solution structure of a DNA kissing complex. *J. Biomol. Struct. Dyn.* **19**, 649–658 (2002).
74. Ding, F. et al. Structure and assembly of the essential RNA ring component of a viral DNA packaging motor. *Proc. Natl Acad. Sci. USA* **108**, 7357–7362 (2011).
75. Aldaz-Carroll, L., Tallet, B., Dausse, E., Yurchenko, L. & Toulmé, J.-J. Apical loop−internal loop interactions: a new RNA−RNA recognition motif identified through in vitro selection against RNA hairpins of the hepatitis C virus mRNA. *Biochemistry* **41**, 5883–5893 (2002).
76. Da Rocha Gomes, S., Dausse, E. & Toulme, J. J. Determinants of apical loop-internal loop RNA-RNA interactions involving the HCV IRES. *Biochem. Biophys. Res. Commun.* **322**, 820–826 (2004).
77. Wei, B., Dai, M. & Yin, P. Complex shapes self-assembled from single-stranded DNA tiles. *Nature* **485**, 623–626 (2012).
78. Ke, Y., Ong, L. L., Shih, W. M. & Yin, P. Three-dimensional structures self-assembled from DNA bricks. *Science* **338**, 1177–1183 (2012).
79. Zhang, F. et al. Complex wireframe DNA origami nanostructures with multi-arm junction vertices. *Nat. Nanotechnol.* **10**, 779–784 (2015).
80. Dietz, H., Douglas, S. M. & Shih, W. M. Folding DNA into twisted and curved nanoscale shapes. *Science* **325**, 725–730 (2009).
81. Han, D. et al. DNA origami with complex curvatures in three-dimensional space. *Science* **332**, 342–346 (2011).
82. Carraher, C. E. Jr *Seymour/Carraher's Polymer Chemistry* 6th edn (CRC Press, 2003).
83. Seeman, N. C. Nucleic acid junctions and lattices. *J. Theor. Biol.* **99**, 237–247 (1982).
84. Feldkamp, U. CANADA: designing nucleic acid sequences for nanobiotechnology applications. *J. Comput. Chem.* **31**, 660–663 (2010).
85. Zuker, M. Mfold web server for nucleic acid folding and hybridization prediction. *Nucleic Acids Res.* **31**, 3406–3415 (2003).
86. Darty, K., Denise, A. & Ponty, Y. VARNA: interactive drawing and editing of the RNA secondary structure. *Bioinformatics* **25**, 1974–1975 (2009).
87. Kao, C., Zheng, M. & Rüdisser, S. A simple and efficient method to reduce nontemplated nucleotide addition at the 3′ terminus of RNAs transcribed by T7 RNA polymerase. *RNA* **5**, 1268–1272 (1999).
88. Tang, G. et al. EMAN2: an extensible image processing suite for electron microscopy. *J. Struct. Biol.* **157**, 38–46 (2007).
89. Pettersen, E. F. et al. UCSF Chimera-a visualization system for exploratory research and analysis. *J. Comput. Chem.* **25**, 1605–1612 (2004).

Data availability

The data supporting the findings of this study are principally within the figures and the associated Supplementary Information. Additional data are available from the authors upon request.

Acknowledgements

D.L. acknowledges the HHMI International Student Research Fellowship. C.W.G. acknowledges a fellowship from the Carlsberg Research Foundation. This work was supported by NSF CAREER Award (DMR-1555361) to Y.W., NIH grant (R01GM102489) to J.A.P., ERC grant (683305) to E.S.A. and NSF grants (CCF-1317694 and CMMI-1636364) and ONR grants (N00014-16-1-2159, N00014-17-1-2610 and N00014-18-1-2649) to P.W.K.R. Cryo-EM experiments were conducted with the Structural Biology Facility at Northwestern University, and we thank J. Remis for assistance. We thank N.-s. Li for synthesizing DFHBI. We thank P. Yin for sharing unpublished results based on bKL and helpful discussions.

Author contributions

D.L. and Y.W. conceived the project. D.L., C.W.G., G.C., Y.S. and M.L. performed the research. C.M., E.S.A., J.A.P., P.W.K.R. and Y.W. supervised the project. D.L., C.W.G., P.W.K.R. and Y.W. wrote the manuscript. All authors analysed the data and commented on the manuscript.

Competing interests

The authors declare no competing interests.

Additional information

Supplementary information is available for this paper at https://doi.org/10.1038/s41557-019-0406-7.

Correspondence and requests for materials should be addressed to P.W.K.R. or Y.W.

Reprints and permissions information is available at www.nature.com/reprints.